

# Exploiting the Steric Effect and Low Dielectric Constant of 1,2-Dimethoxypropane for 4.3 V Lithium Metal Batteries

Eunseok Park,<sup>†</sup> Jongseok Park,<sup>†</sup> Kyunam Lee,<sup>†</sup> Yan Zhao, Tianhong Zhou, Gyuleen Park, Min-Gi Jeong, Minseok Choi, Dong-Joo Yoo, Hun-Gi Jung, Ali Coskun,\* and Jang Wook Choi\*



Read Online

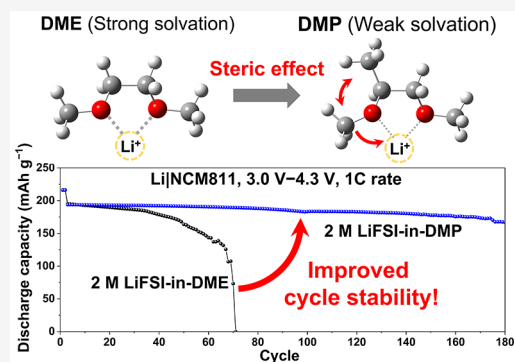
ACCESS |

Metrics & More

Article Recommendations

Supporting Information

**ABSTRACT:** 1,2-Dimethoxyethane (DME) has been widely used as an electrolyte solvent for lithium metal batteries on account of its intrinsic reductive stability; however, its low oxidative stability presents a major challenge for use in high-voltage Li metal batteries (LMBs). In this direction, herein, we introduce a new low-dielectric solvent, 1,2-dimethoxypropane (DMP), as an electrolyte solvent. Compared to DME, DMP has decreased solvation power owing to its increased steric effects, thus promoting anion–Li<sup>+</sup> interactions. This controlled solvation structure of the 2 M LiFSI-in-DMP electrolyte facilitated the formation of an anion-driven, stable interface at the lithium metal anode and oxidative stability for compatibility with widely adopted cathodes to afford LiLiFePO<sub>4</sub> and LiLiNi<sub>0.8</sub>Co<sub>0.1</sub>Mn<sub>0.1</sub>O<sub>2</sub> cells with decent cycling stability. These results imply the usefulness of steric control as an alternative strategy to commonly used fluorination to fine-tune the solvation power and, in general, the design of new solvents for practical lithium metal batteries.



Lithium-ion batteries (LIBs) have been a key enabler in the emergence and radical expansion of the electric vehicle market. However, the ever-increasing demand for LIBs with a higher energy density necessitates the development of “beyond LIB” chemistries to overcome the practical limits of the state-of-the-art intercalation mechanism. Lithium metal, with its high theoretical specific capacity (3860 mAh g<sup>-1</sup>) and low electrochemical potential (−3.04 V vs SHE), is expected to play a key role in replacing intercalation-based anode materials in this technological direction.<sup>1,2</sup> In this respect, the scientific community has shown growing interest in solving the critical issues presented by lithium metal batteries (LMBs), such as their poor cycle life, dendritic growth, and electrolyte consumption during cycling. These problems originate from the low thermodynamic stability of conventional liquid electrolytes toward Li metal, which leads to the formation of an intrinsically unstable interface.<sup>3–5</sup> In this regard, various strategies, including the employment of artificial solid electrolyte interphase (SEI) layers,<sup>6,7</sup> electrode designs,<sup>8,9</sup> electrolyte additives,<sup>10–12</sup> and solid-state electrolytes<sup>13</sup> have been developed. Among these approaches, electrolyte engineering has gained much interest because it is readily adaptable in cell manufacturing. Critically, the solvation structure of the electrolyte has been shown to have a profound impact on the chemical composition and physicochemical properties of

the SEI layer.<sup>14</sup> The solvation structure of electrolytes depends strongly on the molecular structure of the solvent/cosolvent and salt concentration and can be classified as solvent-separated ion pairs (SSIP), contact ion pairs (CIP), and aggregated ions (AGG).<sup>15,16</sup> During Li plating, Li<sup>+</sup>-coordinating solvents and anions accumulate in the vicinity of the reducing lithium metal surface, followed by their reductive decomposition to form the SEI. In this connection, CIP and AGG structures induce the formation of a robust inorganic-rich SEI owing to the preferential decomposition of the anions.<sup>17,18</sup>

An effective and intuitive strategy to raise the levels of CIPs and AGGs in electrolytes is to increase the salt concentrations to near the solubility limits and to maximize the salt-to-solvent ratio (Figure S1). These high-concentration electrolytes (HCEs) induce the formation of an anion-driven, inorganic-rich SEI layer on lithium metal to enhance the Coulombic

Received: September 4, 2022

Accepted: October 31, 2022

Published: December 4, 2022

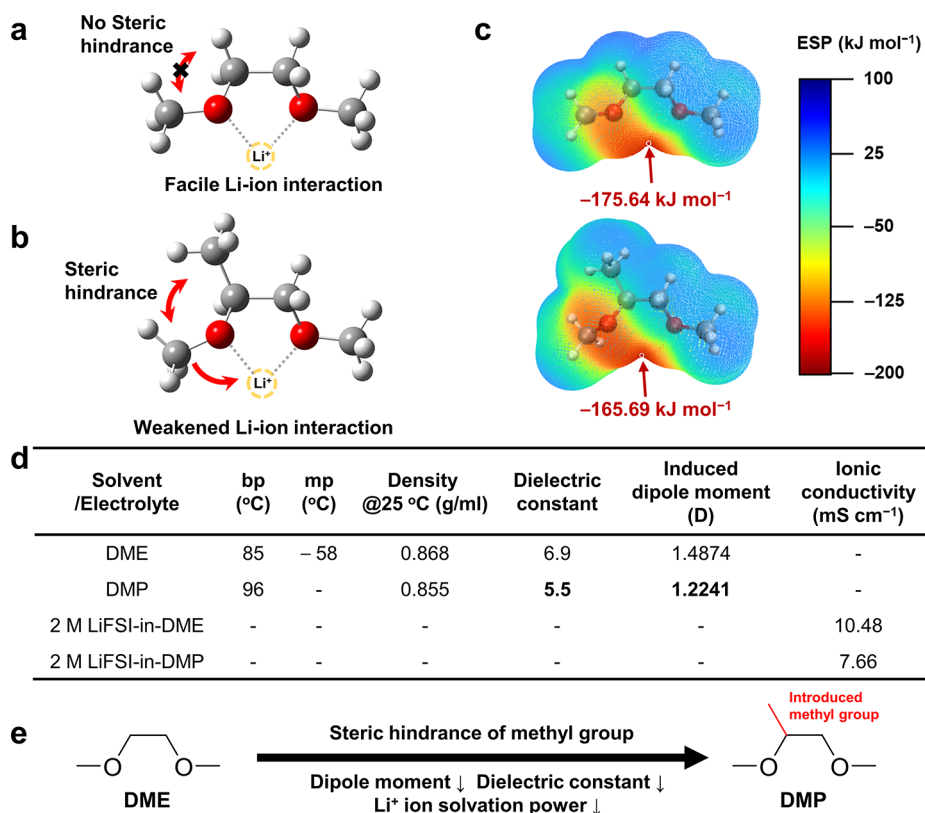


Figure 1. Schematic illustration of steric hindrance and interaction with Li-ion for (a) DME and (b) DMP. (c) Calculated minimum electrostatic potentials (ESPs) of DME and DMP (see also Figure S4). (d) Schematic diagram of solvation power according to solvent structure. (e) Properties of solvents and electrolytes.

efficiency.<sup>19</sup> Furthermore, the formation of a robust cathode-electrolyte-interphase (CEI) on the positive electrode is also beneficial in terms of diminishing the oxidative decomposition of electrolyte components.<sup>20</sup> However, apart from their high cost, HCEs are highly viscous and have low ionic conductivity, which result in high overpotential and impaired rate performance during battery cycling.<sup>16</sup> In addition, localized high-concentration electrolytes (LHCEs) consisting of the combination of a noncoordinating diluent and a strongly coordinating solvent have also been suggested to resolve the aforementioned shortcomings of HCEs by maintaining high concentrations of clusters containing CIPs and AGGs in the electrolyte at low bulk salt concentrations. In this sense, various highly fluorinated diluents of which the corresponding LHCEs proved to be effective in stabilizing the SEI layer have been reported.<sup>21–24</sup>

Recently, weakly coordinating solvents (WCSs) have been investigated as an alternative to HCEs and LHCEs. The Li<sup>+</sup>-solvation power of WCSs can be tuned to induce the formation of CIPs and AGGs in the electrolytes to form an inorganic-rich stable SEI.<sup>25–28</sup> The solvating power of solvents can be roughly estimated from the values of the dipole moment and dielectric constant, and these parameters are generally proportional to each other. These two parameters, which could also be considered to be electrostatic factors, are representative indicators of the extent to which a solvent can stabilize a charged ion;<sup>29,30</sup> the lower these values are, the lower the solvating power will be to induce the formation of additional CIP and AGG-abundant solvation structures in the electrolyte. In the same context, various low-dielectric solvents have been

proposed and shown to effectively operate in batteries with Li metal<sup>31</sup> and graphite<sup>32</sup> anodes.

Herein, we introduce commercially available 1,2-dimethoxypropane (DMP) as a weakly coordinating solvent for LMB cells. Motivated by the higher stability of ether-based electrolytes to Li metal than their carbonate-based counterparts, the molecular structure of the commercial ether-based solvent, 1,2-dimethoxyethane (DME), was simply modified to effectively weaken the solvating power and induce CIP- and AGG-rich solvation structures. These solvation structures resulted in the formation of an inorganic-rich robust SEI during Li plating, which enhanced the cyclability of Li/Cu and Li/Li cells. Moreover, the use of DMP also largely addressed the unwanted incompatibility of ethers with high-voltage cathodes (e.g., LiNi<sub>0.8</sub>Co<sub>0.1</sub>Mn<sub>0.1</sub>O<sub>2</sub> (NCM811)) by manipulating the electrostatic properties of the electrolyte. The beneficial effect of DMP in full-cell settings containing popular nickel (Ni)-rich layered oxide cathodes was demonstrated.

**Molecular Design and Li<sup>+</sup> Solvation Structure of Electrolytes.** Many ether-based electrolytes, such as a solution of LiFSI in DME, have low oxidative stability at high voltages (>4 V vs Li/Li<sup>+</sup>) and are known to corrode aluminum (Al). Both of these disadvantageous properties are linked to their inferior cycling performance. To address these challenges, we propose to structurally modify the ether-based solvent such that both its physicochemical properties and practical application are taken into account. Our design principles involved the following: (1) the intrinsic reductive stability of DME should not be seriously hampered; (2) the high ionic conductivity should be maintained; (3) the Li<sup>+</sup>-solvating power of the solvent should be tuned to allow more anions to reside

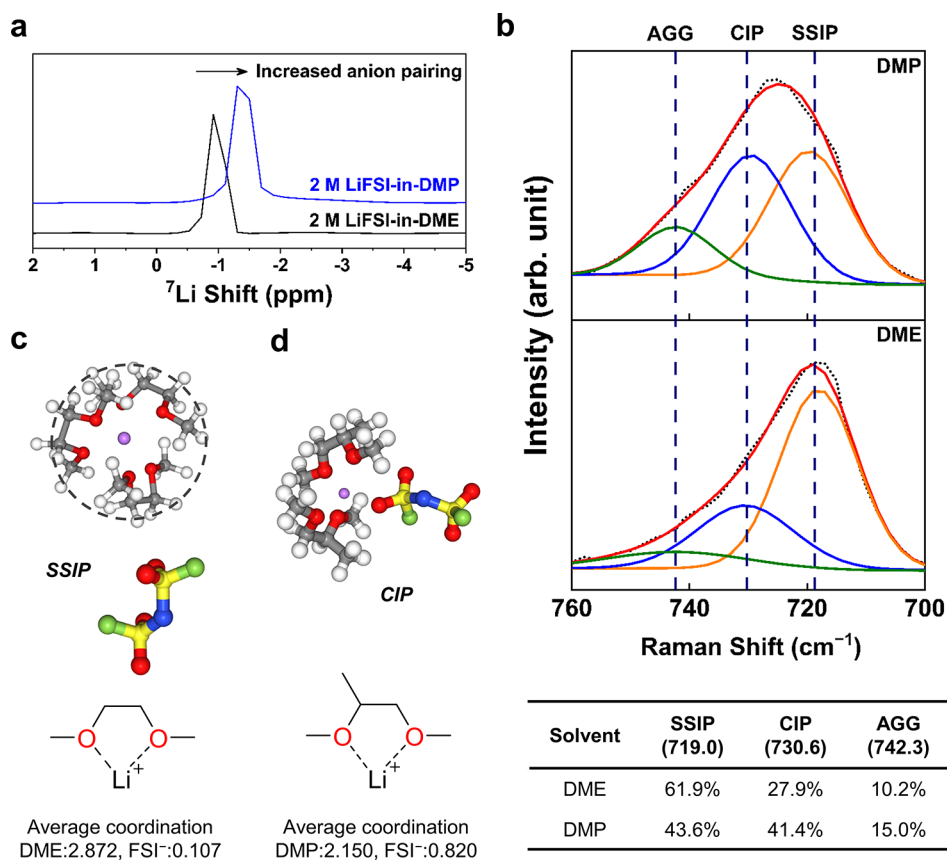


Figure 2. (a)  $^7\text{Li}$  NMR spectra of 2 M LiFSI-in-DME and 2 M LiFSI-in-DMP. (b) Raman spectra of 2 M LiFSI-in-DME and 2 M LiFSI-in-DMP. Most probable solvation structures of the first  $\text{Li}^+$  solvation sheath of (c) DME and (d) DMP electrolytes from MD simulations (see also Figures S5 and S6).

around  $\text{Li}^+$ ; (4) compatibility with the Al current collector should be warranted, and finally (5) the designed solvent should be readily available for practical adoption. With these design principles in mind, we introduced commercially available DMP as a weakly solvating electrolyte solvent. Although the additional weakly electron-donating methyl group increases the overall electron-density of the system, its steric effect limits the interaction of the DMP molecule with  $\text{Li}^+$  ions, thus providing a way in which to control the solvation power (Figures 1a,b and S2). Compared to DME, the carbon atom of the methoxy group in closer proximity to the additional methyl group in DMP is pushed closer to the  $\text{Li}^+$  ion due to the steric hindrance between the methyl and methoxy groups (arrows in Figure 1b). This steric effect lowers the solvation power of DMP compared to DME. Consequently, this steric effect would also be expected to decrease the dipole moment and dielectric constant. In this line, we reasoned that the dipole moment and dielectric constant along with the molecular structure could be used as representative parameters because the dielectric constant dictates the degree of interaction between the charged ion and solvent molecules; namely, it determines the strength of coordination. For most molecules, these two parameters are by and large proportional to the strength of coordination, with  $\text{H}_2\text{O}$  being a notable exception because of its high dielectric constant and low dipole moment.<sup>33</sup> Based on this rationale, molecules with low dipole moments are expected to have weak solvating power, thus augmenting the relative portions of CIPs and AGGs in the electrolyte. Although DME is a nonpolar solvent, the

imposition of an electric field would lead to the gauche conformation as in Figure 1a, and this would induce a dipole moment. This induced dipole moment gives rise to a net negative charge on the oxygen side and a net positive charge on the ethane side. However, in the case of DMP, the steric effect pushes the methoxy carbon away from the ethane backbone to reduce the overall charge separation (Figure 1b). Therefore, we expected the steric effect to decrease the dipole moment and dielectric constant of DMP and thereby its solvation power compared to DME.

In an attempt to confirm our hypothesis, the dipole moments of DME and DMP were calculated using density functional theory (DFT) calculations (Figure S3). To precisely reflect the solvation environments in the calculations, the molecular conformations of the solvents alone were optimized to resemble their solvation structures in which they coordinate with one  $\text{Li}^+$  ion (see Experimental Methods in the Supporting Information). In this optimized conformation, the dipole moment of DME with  $C_2$ -symmetry has a value of 1.4874 D (Figures 1d and S3a). DMP, with a methyl group attached to DME, has an asymmetrically shifted and lower dipole moment of 1.2241 D owing to reduced intramolecular charge separation as described above (Figures 1d and S3b). In addition, the dielectric constants were experimentally measured to be 6.9 for DME and 5.5 for DMP, consistent with the calculated dipole moment values (Figure 1d). Therefore, the DFT calculations and experimental measurements support our conjecture that the targeted methylation of DME effectively reduces the dipole

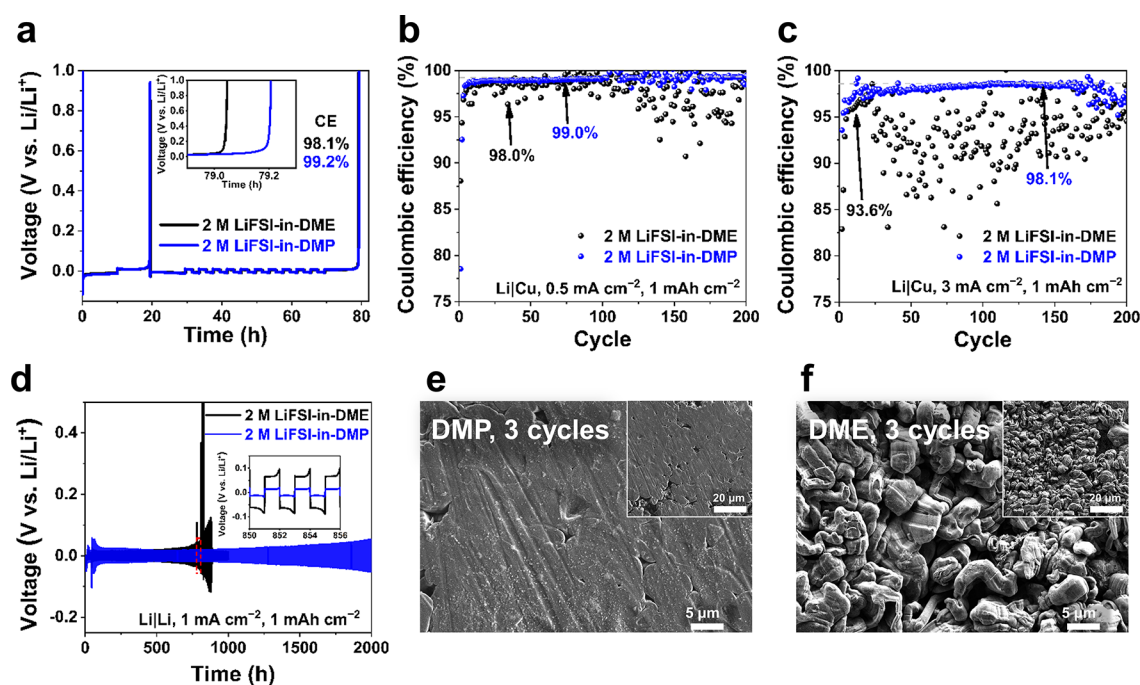


Figure 3. (a) Aurbach measurement of Li metal CEs in Li|Cu cells. CEs of Li|Cu cells cycled at (b)  $0.5 \text{ mA cm}^{-2}$  and (c)  $3 \text{ mA cm}^{-2}$ . (d) Cycling performance of Li|Li symmetric cells. Scanning electron microscopy (SEM) images of Li surface using (e) 2 M LiFSI-in-DMP and (f) 2 M LiFSI-in-DME at  $0.5 \text{ mA cm}^{-2}$ ,  $1 \text{ mAh cm}^{-2}$  after 3 cycles (see also Figure S9).

moment and dielectric constant to realize the low-dielectric solvent DMP as intended (Figure 1e).

Although the dipole moment and dielectric constant were strategically decreased, it was still preferable to verify whether the electrostatic interaction of DMP with  $\text{Li}^+$  ions was weakened compared to that of DME. DFT calculations were also employed to evaluate the electrostatic potentials (ESPs) of both DME and DMP (Figures 1c and S4). The more negative the value of the minimum ESP is, the stronger the solvent interaction with the cation is expected to be. Accordingly, the minimum ESP of DMP was calculated to be  $-165.69 \text{ kJ mol}^{-1}$ , which is smaller in absolute value than that of DME ( $-175.64 \text{ kJ mol}^{-1}$ ), suggesting that the interaction of DMP with  $\text{Li}^+$  ions, and thus the solvating power, weakens compared to DME. The methoxy carbon of DMP, which is located closer to the ESP minimum than that of DME, can add to the effect of the positive electrostatic potential, lowering the absolute value of the minimum ESP despite the presence of the additional electron-donating methyl group.

The weaker solvating power of DMP compared to DME was further verified by experimental characterizations and molecular dynamics (MD) simulations (Figure 2). In addition to the molecular properties of the individual solvents discussed thus far, the corresponding electrolytes, namely, 2 M LiFSI-in-DME and 2 M LiFSI-in-DMP were considered in subsequent analyses to understand their solvation properties. First, the  $^7\text{Li}$  NMR spectra of these electrolytes were recorded (Figure 2a). The  $^7\text{Li}$  peak of 2 M LiFSI-in-DMP was shifted upfield compared to that of 2 M LiFSI-in-DME. This result indicates that a greater number of anions surround the  $\text{Li}^+$  ion in DMP-based electrolytes than in their DME analogues owing to the increased electron density surrounding the  $^7\text{Li}$  nuclei.<sup>34</sup> Additionally, Raman spectroscopy was utilized (Figure 2b) to further probe the solvation structure. It should be noted that the solvating power of a solvent has a profound impact on the

nature and distribution of ion pairs in the electrolyte. The Raman spectrum of 2 M LiFSI-in-DME is characterized by a high-intensity peak at  $719.0 \text{ cm}^{-1}$ , indicating that most anions are present as SSIPs. In contrast, the Raman peaks of 2 M LiFSI-in-DMP at  $730.6$  and  $742.3 \text{ cm}^{-1}$  were of a significantly higher intensity owing to the formation of CIPs and AGGs, respectively. The relative compositions of ionic species were also evaluated quantitatively by areal analysis of the peaks on the deconvoluted Raman spectra. In comparison, 61.9% of anions were present as SSIPs in 2 M LiFSI-in-DME, whereas only 43.6% of anions were found to have formed SSIPs in 2 M LiFSI-in-DMP. The most probable solvation structures were also constructed by conducting MD simulations (Figure 2c,d). The average numbers of solvent molecules and anions coordinating with each  $\text{Li}^+$  ion in the 2 M LiFSI-in-DME electrolyte were 2.872 and 0.107, respectively, revealing SSIPs as the main solvation configuration (Figures 2c and S5). On the other hand, in the 2 M LiFSI-in-DMP electrolyte, 2.150 DMP molecules and 0.820 FSI<sup>-</sup> anions coordinate with each  $\text{Li}^+$  ion on average. This is in good agreement with the NMR and Raman analyses, pointing to the formation of CIP- and AGG-dominant solvation structures (Figure 2d and S6). It should be noted that the maximum coordination number of DMP to  $\text{Li}^+$  ion was 3, which was the same as that of DME (Figures S5b, S6b, and S7). This indicates that the methyl group of DMP, on the opposite side of its coordination site, effectively reduced the solvating power without largely altering the  $\text{Li}^+$  ion binding structure.

**Performance and Morphology Analyses in Various Cell Configurations.** The CIP- and AGG-enriched solvation structure of the 2 M LiFSI-in-DMP electrolyte prompted us to investigate the electrochemical performance of this electrolyte in the Li|Cu half-cell and in Li|Li symmetric and full-cell configurations by pairing with both LFP and NCM811 cathodes. To probe the Coulombic efficiency (CE) in the Li|

Cu half-cell configuration, Aurbach's method was used.<sup>35</sup> The 2 M LiFSI-in-DMP electrolyte had (Figure 3a) higher CE of 99.2% compared to 98.1% of the conventional 2 M LiFSI-in-DME electrolyte. The improved cathodic reversibility of the DMP-based electrolyte also served to improve the cycling of Li/Cu half-cells (Figures 3b,c and S8a) with higher average CE than the DME counterpart at 0.5 mA cm<sup>-2</sup> (99.0% vs 98.0%), 1.0 mA cm<sup>-2</sup> (98.5% vs 94.8%), and 3.0 mA cm<sup>-2</sup> (98.1% vs 93.6%). SEM analysis was used to probe the morphology of the plated Li after half-cell cycling (Figures 3e,f, S8b,c, and S9). Irrespective of the applied current density, denser and laterally larger Li deposits were observed after 3 and 20 cycles with the 2 M LiFSI-in-DMP electrolyte (Figures 3e, S8b, and S9a,b), while the Li deposits in the DME equivalent had a porous, thin, and mossy appearance (Figures 3f, S8c, and S9c,d), which could amplify consumption of the electrolyte upon cycling. In addition, the prolonged cycling results of the 2 M LiFSI-in-DMP electrolyte compared to those of the 2 M LiFSI-in-DME electrolyte in Li/Li symmetric cells were also in good agreement with the CE results (Figure 3d). In contrast to the more than 2000 h of stable cycling observed with 2 M LiFSI-in-DMP at 1 mA cm<sup>-2</sup> and 1 mAh cm<sup>-2</sup>, in the same cell setting, the cell containing 2 M LiFSI-in-DME experienced a severe increase in overpotential and ceased to operate after nearly 900 h. The enhanced performance of the DMP-based electrolyte in terms of both the CE and cyclability of symmetric cells reflected its effect on the formation of a stable interface with the anode, as was additionally confirmed by cyclic voltammetry analysis with Li/Li cells (Figure S10). The reductive decomposition of electrolyte components before Li plating can be detected in the potential range of 0.0–2.0 V (vs Li/Li<sup>+</sup>). As shown in Figure S10, compared to its DME counterpart, the cathodic current densities of 2 M LiFSI-in-DMP were significantly lower during repeated CV cycles. In the initial potential scan from open-circuit voltage (OCV) to 0 V, 2 M LiFSI-in-DME showed higher negative current density compared to that of 2 M LiFSI-in-DMP, indicating more serious electrolyte decomposition of 2 M LiFSI-in-DME in forming the initial SEI. This difference can be explained by the inorganic-rich, robust SEI formed with 2 M LiFSI-in-DMP that prevents further electrolyte decomposition in the first and subsequent cycles. This is indicative of decreased reductive decomposition of the electrolyte components after the initial formation of a robust inorganic-rich SEI layer as a result of CIP- and AGG-enriched solvation structures.

As a consequence of the enhanced reversibility of 2 M LiFSI-in-DMP in Li plating/stripping cycles, full cells with the 2 M LiFSI-in-DMP electrolyte could also be observed to undergo stable cycling, in line with the half-cell measurements. Figure 4a demonstrates the full cell performance of the DMP electrolyte in a Li/LiFePO<sub>4</sub> (LFP) coin-cell with 40 μm thick Li foil. It is worth noting that LFP has recently been in the spotlight as a competitive cathode material by virtue of its excellent cyclability, thermal stability, low cost, and environmental friendliness.<sup>36,37</sup> After 385 charge/discharge cycles at C/2, 97.7% of its initial capacity was retained with the 2 M LiFSI-in-DMP electrolyte, whereas the cell with 2 M LiFSI-in-DME ceased to operate after 230 cycles. Furthermore, full cells with 40 μm thick Li foil and high voltage NCM811 cathodes (~4.3 V vs Li/Li<sup>+</sup>) clearly delivered superior cycling performance with 2 M LiFSI-in-DMP compared to its DME counterpart (Figures 4b,c and S11). The 2 M LiFSI-in-DME electrolyte caused the Li/NCM811 cell to experience a major

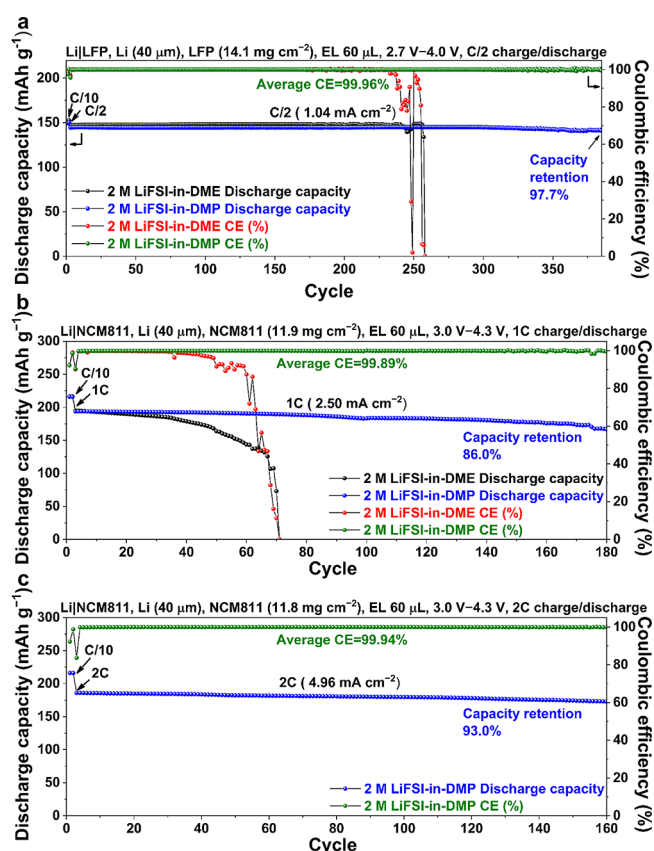


**Figure 4.** Cycling performance of (a) Li/LFP full cells at 0.5C and Li/NCM811 full cells at (b) 1C and (c) 2C after 2 formation cycles at 0.1C with 2 M LiFSI-in-DME and 2 M LiFSI-in-DMP. The average CE refers to the average value after the two initial cycles.

capacity loss (~50% capacity retention) after 70 cycles at 1C (Figures 4b and S11a), whereas 2 M LiFSI-in-DMP sustained more than 180 cycles with 86.0% capacity retention when cycled at 1C (Figures 4b and S11b). The decent capacity retention with 2 M LiFSI-in-DMP was maintained even at a high current density of 2C, ~5 mA cm<sup>-2</sup> (Figure 4c). The superior cyclability of 2 M LiFSI-in-DMP in Li/NCM811 stems from the reversible Li plating/stripping as discussed hitherto as well as the enhanced anodic stability offered by the designed electrolyte as verified by linear sweep voltammetry (LSV) and a potentiostatic polarization test (Figure S12). LSV tests with Li/Li cells (Figure S12a) demonstrated that the peak position associated with the anodic current by electrolyte decomposition was greatly delayed for 2 M LiFSI-in-DMP (~4.5 V vs Li/Li<sup>+</sup>) compared to 2 M LiFSI-in-DME (~4.2 V vs Li/Li<sup>+</sup>). Similarly, potentiostatic polarization tests with Li/NCM811 cells revealed severe anodic decomposition for 2 M LiFSI-in-DME at 4.4–4.5 V, whereas the anodic current was largely suppressed with the 2 M LiFSI-in-DMP electrolyte even at 4.5 V (Figure S12b). Both the LSV and potentiostatic polarization measurements indicated that the DMP-based electrolyte is less susceptible to oxidative instability as a result of its weakened solvation power compared to the DME-based electrolyte. By virtue of its enhanced interfacial stability, the 2 M LiFSI-in-DMP electrolyte had superior rate capability (Figure S13) despite its slightly lower ionic conductivity (Figure 1d). Also, the 2 M LiFSI-in-DMP electrolyte demonstrated decent cyclability with a high loading NCM811 cathode (20.3 mg

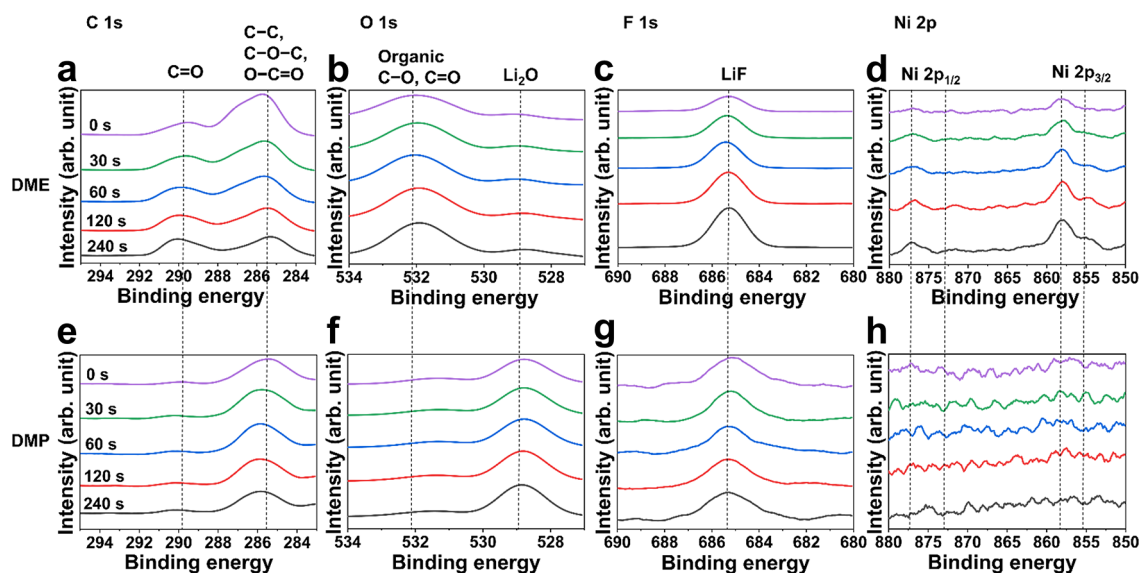


Figure 5. Ex situ interfacial analysis of Li metal anode surface in Li|NCM811 full cells. X-ray photoelectron spectroscopy (XPS) depth profiles of Li metal surface after 3 cycles with (a–d) 2 M LiFSI-in-DME and (e–h) 2 M LiFSI-in-DMP electrolytes: (a and e) C 1s spectra, (b and f) O 1s spectra, (c and g) F 1s spectra, and (d and h) Ni 2p spectra.

$\text{cm}^{-2}$ ) at a high current density of  $4.27 \text{ mA cm}^{-2}$  (1C rate) (Figure S14).

**Interface Characterization.** To understand the origin of the enhanced electrochemical performance of the 2 M LiFSI-in-DMP electrolyte, X-ray photoelectron spectroscopy (XPS) analysis was used to probe the compositions of both the SEI and CEI layers formed after 3 cycles in Li|NCM811 full cells with the 2 M LiFSI-in-DME and 2 M LiFSI-in-DMP electrolytes. The XPS depth profiles in Figure 5a–h inform the distributions of the SEI elements at various depths below the surface. The peaks of the O 1s spectrum of the SEI layer formed by 2 M LiFSI-in-DME (Figure 5b) were highly concentrated at 532 eV with varying intensities indicating large amounts of organic C–O and C=O species with a nonuniform distribution along the depth. In contrast, the O 1s profiles of the SEI layer of 2 M LiFSI-in-DMP exhibited intense  $\text{Li}_2\text{O}$  peaks at 529 eV with depth-independent uniformity (Figure 5f).<sup>38,39</sup> Similar to the O 1s profiles, the F 1s spectra of the 2 M LiFSI-in-DME electrolyte indicated its inhomogeneous SEI composition along the depth (Figure 5c); the LiF content detected at 685 eV in the same SEI layer was found to gradually increase with increasing depth. In contrast, the SEI layer on Li metal with 2 M LiFSI-in-DMP had uniform and depth-independent  $\text{Li}_2\text{O}$  and LiF distributions (Figure 5f, g). The intensities of the peaks at 290 eV on the C 1s spectrum, assigned to organic carbon species, were much lower for the DMP-based electrolyte compared to the DME-based electrolyte. It should be noted that, because the C 1s peaks at 284–288 eV in the XPS analysis are associated with inevitable carbon contamination, we focused on the peaks related to the C=O species at 290 eV (Figure 5a,e).<sup>40–42</sup> These results are supportive of the formation of an inorganic-rich, anion-derived, homogeneous SEI layer in the case of 2 M LiFSI-in-DMP, which stems from the CIP- and AGG-enriched solvation structures. Interestingly, we also detected Ni species in the SEI with the 2 M LiFSI-in-DME electrolyte at 858 eV on the Ni 2p spectrum whereas no obvious Ni species were detected in the case of 2 M LiFSI-in-DMP (Figure 5d,h). Considering that the only plausible source of Ni is the cathode, this result infers that

the NCM811 cathode underwent more significant degradation with 2 M LiFSI-in-DME involving the dissolution of transition metal ions. This can presumably be attributed to the inability of the CEI layer to protect the cathode surface and the vulnerability of the electrolyte to oxidation. The suppressed degradation of the cathode in the 2 M LiFSI-in-DMP electrolyte was evident from the XPS results of the cycled NCM811 cathodes (Figure S15). The XPS O 1s spectrum of the CEI formed by the 2 M LiFSI-in-DME electrolyte contained high intensity organic C–O and C=O peaks (Figure S15b), whereas higher metal oxide contents were observed in the case of 2 M LiFSI-in-DMP (Figure S15d). The F 1s spectrum showed that the LiF content of the CEI of 2 M LiFSI-in-DME increased as the depth below the surface increased, indicating the accumulation of organic species in its outer CEI layer. In contrast, the LiF content in the CEI layer was distributed rather homogeneously with 2 M LiFSI-in-DMP (Figure S15e,f). Accordingly, it could be concluded that the robust CEI layer formed by 2 M LiFSI-in-DMP effectively suppressed further decomposition of the organic solvents and suppressed the dissolution of Ni from the cathode. The CEI layers of LFP cathodes were also analyzed by in-depth XPS after 3 cycles in the Li|LFP cell setting (Figure S16). Owing to the lower redox potential ( $E_0 = 3.45 \text{ V vs Li/Li}^+$ )<sup>37</sup> of LFP, the CEI compositions were not much different between the two electrolytes. Therefore, the enhanced cyclic stability of the Li LFP cells with 2 M LiFSI-in-DMP mainly stems from the anode side based on more reversible Li plating/stripping.

**Oxidation Stability and Degradation Analysis.** With regard to the cathode interface, the apparent ability of the DMP-based electrolyte to suppress the degradation of the NCM811 cathode was verified by XRD analysis. To this end, the crystallinity of the cathodes was evaluated after 20 cycles in different electrolytes (Figure 6a). The cathode cycled with the 2 M LiFSI-in-DME electrolyte had a poorly resolved diffraction pattern, in contrast to the peaks of the cathode cycled with the 2 M LiFSI-in-DMP electrolyte. Moreover, the two cathodes could also be differentiated by the intensity ratio of the (003) and (104) peaks, namely,  $I(003)/I(104)$ , which

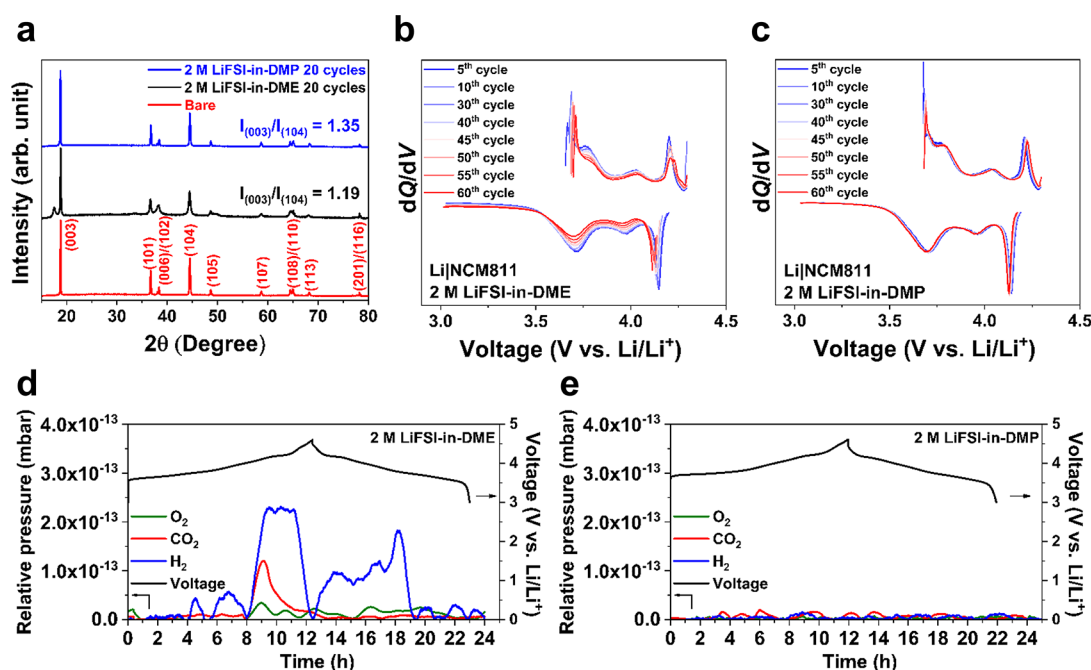


**Figure 6.** (a) X-ray diffraction (XRD) patterns of NCM811 from Li|NCM811 full cells after 20 cycles.  $dQ/dV$  profiles of Li|NCM811 full cells at different cycles with the (b) 2 M LiFSI-in-DME and (c) 2 M LiFSI-in-DMP electrolytes. Differential electrochemical mass spectrometry (DEMS) analysis of the evolved gases during the charge and discharge of Li|NCM811 full cells in the range of 3.0–4.6 V with the (d) 2 M LiFSI-in-DME and (e) 2 M LiFSI-in-DMP electrolytes. The left axis represents the detected gas pressure of  $O_2$  (green line),  $CO_2$  (red line), and  $H_2$  (blue line). The right axis corresponds to the potential of the charging and discharging step (black line).

serves as an indicator of the degree of cation mixing in layered oxide cathodes. The decrease in the  $I(003)/I(104)$  ratio indicates the movement of  $Ni^{2+}$  ions to the layered  $Li^+$  sites, which is accompanied by interfacial destabilization involving the dissolution of transition metal ions.<sup>43,44</sup> The intensity ratio  $I(003)/I(104)$  of the cathode cycled with 2 M LiFSI-in-DMP was 1.35, which is clearly higher than the 1.19 of 2 M LiFSI-in-DME, verifying the greater stability of the host framework when the DMP-based electrolyte was used. In addition to the XRD pattern, the  $dQ/dV$  profiles of Li|NCM811 full cells were also recorded during cycling to examine the states of health (SoH) of the cathodes in real time (Figure 6b,c). NCM811 experiences consecutive phase transitions ( $H1 \rightarrow M \rightarrow H2 \rightarrow H3$ ) during charging, which are electrochemically reflected on the  $dQ/dV$  profiles.<sup>45</sup> At the fifth cycle, sharp peaks assigned to different phase transition steps were observed for both electrolytes, implying that, in both cases, the active materials were in a good condition. These clearly observable phase transitions of the cathodes gradually broadened or shifted more significantly with 2 M LiFSI-in-DME, whereas the cathode with 2 M LiFSI-in-DMP sustained sharp peaks during the same cycling period. Remarkably, the  $H2 \rightarrow H3$  transition at  $\sim 4.2$  V, which is notoriously responsible for the decay of NCM811 as a result of abrupt lattice contraction in the  $c$ -direction,<sup>46</sup> was reversibly retained during subsequent cycles with the 2 M LiFSI-in-DMP electrolyte. Additional verification of the improved interfacial stability of the DMP-based electrolyte was obtained by conducting differential electrochemical mass spectrometry (DEMS) analysis of the evolution of gaseous byproducts during the initial cycle (Figure 6d,e). In the Li|NCM811 full cell with the 2 M LiFSI-in-DME electrolyte,  $H_2$  gas started to evolve at  $\sim 3.7$  V, and this became vigorous above  $\sim 4.0$  V along with the generation of  $CO_2$  and  $O_2$ . In stark contrast, for the Li|NCM811 cell with 2

M LiFSI-in-DMP, negligible evolution of these gases was detected even until deep delithiation at 4.6 V, indicating enhanced interfacial stability. Above 4.3 V, the oxidation state of Ni is known to change to close to +4, triggering oxygen evolution from the crystal lattice to reduce unstable  $Ni^{4+}$  to stable  $Ni^{2+}$ , which induces cation mixing in proximity to the surface of NCM811 particles.<sup>47</sup> The  $Ni^{2+}$  formed during this cation mixing process is more soluble than  $Ni^{3+}$  or  $Ni^{4+}$ , rendering the transition metal ions more vulnerable to dissolution by high dielectric, strongly solvating solvents.<sup>48–50</sup> In this regard, the DMP-based electrolyte with its low dielectric constant is more beneficial for mitigating transition metal dissolution toward protecting the crystallinity of the cathode.

On the other hand, LiFSI in ether-based electrolytes has long been known to induce corrosion of the Al current collector. With this critical drawback in mind, we performed potentiostatic polarization tests for both of the electrolytes in Li|Al cells (Figures S17–S20). With 2 M LiFSI-in-DME, the anodic current began to flow as soon as the potential was applied to increase exponentially both at 4.3 and 4.4 V (Figure S17). By contrast, no apparent anodic current was detected at 4.3 and 4.4 V for the Li|Al cell with the 2 M LiFSI-in-DMP electrolyte, in which case the anodic current started to flow slowly at 4.5 V (Figure S17). A great number of pits were observed on the Al surface of the 2 M LiFSI-in-DME cell after 6 h of applied potential as a signature of corrosion, and the corrosion became even more severe after 72 h (Figures S18a and S19a). In stark contrast, corroded sites on the surface of Al foil in contact with 2 M LiFSI-in-DMP were observed only at 4.5 V (Figures S18b and S19b). This difference in the oxidative dissolution of the Al current collector was also attributed to the different dielectric constants of DME and DMP. As shown in several studies, corrosion byproducts, in our case  $Al(FSI)_3$ , are

readily dissolved in an electrolyte comprising high dielectric solvents at high voltages, whereas their dissolution is much lower in low-dielectric solvents, thus enabling effective passivation of the Al surface.<sup>51–55</sup>

To summarize, an ether-based low-dielectric solvent, 1,2-dimethoxypropane (DMP), was designed to reliably operate LMBs containing high-voltage cathodes. The solvating power of DME was modified by fine-tuning the structure by incorporating increased steric hindrance. This slight alteration from DME to DMP induced the formation of an anion-driven SEI layer, enabling highly reversible plating/stripping behavior with Li metal. Furthermore, the oxidative stability of 2 M LiFSI-in-DMP resulted in forming a uniform and robust CEI layer on the cathode surface, explaining the observed enhanced full-cell performance. The low dielectric constant of DMP also largely inhibited transition metal dissolution from NCM811 active particles and corrosion of the Al current collector. In combination, all of these beneficial features enabled the Lil NCM811 full cell to operate for more than 160 cycles at a high current density ( $\sim 5 \text{ mA cm}^{-2}$ ) with Li foil of a limited thickness ( $40 \mu\text{m}$ ). Our findings highlight the importance of the fine structural manipulation of electrolyte solvents to adjust the solvation structure toward advancing LMBs to practically viable options. Moreover, the structurally fine-tuned solvents could be applied beyond LMBs such as LIBs operating under extreme fast charging conditions or at low temperatures.<sup>56–59</sup>

## ■ ASSOCIATED CONTENT

### SI Supporting Information

The Supporting Information is available free of charge at <https://pubs.acs.org/doi/10.1021/acseenergylett.2c02003>.

Experimental details, DFT and MD calculation results, SEM images, XPS results, and additional electrochemical tests (PDF)

## ■ AUTHOR INFORMATION

### Corresponding Authors

Ali Coskun – Department of Chemistry, University of Fribourg, Fribourg 1700, Switzerland; [orcid.org/0000-0002-4760-1546](https://orcid.org/0000-0002-4760-1546); Email: [ali.coskun@unifr.ch](mailto:ali.coskun@unifr.ch)

Jang Wook Choi – School of Chemical and Biological Engineering and Institute of Chemical Processes, Seoul National University, Seoul 08826, Republic of Korea; [orcid.org/0000-0001-8783-0901](https://orcid.org/0000-0001-8783-0901); Email: [jangwookchoi@snu.ac.kr](mailto:jangwookchoi@snu.ac.kr)

### Authors

Eunseok Park – School of Chemical and Biological Engineering and Institute of Chemical Processes, Seoul National University, Seoul 08826, Republic of Korea; [orcid.org/0000-0001-9756-9532](https://orcid.org/0000-0001-9756-9532)

Jongseok Park – School of Chemical and Biological Engineering and Institute of Chemical Processes, Seoul National University, Seoul 08826, Republic of Korea

Kyunam Lee – School of Chemical and Biological Engineering and Institute of Chemical Processes, Seoul National University, Seoul 08826, Republic of Korea

Yan Zhao – Department of Chemistry, University of Fribourg, Fribourg 1700, Switzerland; [orcid.org/0000-0001-5324-5050](https://orcid.org/0000-0001-5324-5050)

Tianhong Zhou – Department of Chemistry, University of Fribourg, Fribourg 1700, Switzerland; [orcid.org/0000-0002-9537-8465](https://orcid.org/0000-0002-9537-8465)

Gyuleen Park – School of Chemical and Biological Engineering and Institute of Chemical Processes, Seoul National University, Seoul 08826, Republic of Korea

Min-Gi Jeong – Energy Storage Research Center, Korea Institute of Science and Technology (KIST), Seoul 02792, Republic of Korea

Minseok Choi – School of Chemical and Biological Engineering and Institute of Chemical Processes, Seoul National University, Seoul 08826, Republic of Korea

Dong-Joo Yoo – School of Mechanical Engineering, Korea University, Seoul 02841, Republic of Korea; [orcid.org/0000-0001-5656-8613](https://orcid.org/0000-0001-5656-8613)

Hun-Gi Jung – Energy Storage Research Center, Korea Institute of Science and Technology (KIST), Seoul 02792, Republic of Korea; [orcid.org/0000-0002-2162-2680](https://orcid.org/0000-0002-2162-2680)

Complete contact information is available at:

<https://pubs.acs.org/10.1021/acseenergylett.2c02003>

### Author Contributions

†E.P., J.P., and K.L. contributed equally to this work.

### Notes

The authors declare no competing financial interest.

## ■ ACKNOWLEDGMENTS

J.W.C. acknowledges the support from the National Research Foundation of Korea (NRF) (NRF-2021R1A2B5B03001956); the Technology Innovation Program (20012341) funded by the Ministry of Trade, Industry & Energy (MOTIE) of Korea; and generous support from the Institute of Engineering Research (IOER) and Research Institute of Advanced Materials (RIAM) at Seoul National University. A.C. and J.W.C. acknowledge the support from the Swiss National Science Foundation (SNF) (Sinergia, CRSIIS\_202296). A.C. also acknowledges the Global Visiting Fellowship from the National Research Foundation of Korea (NRF) through the BK21 Program.

## ■ REFERENCES

- (1) Lin, D.; Liu, Y.; Cui, Y. Reviving the lithium metal anode for high-energy batteries. *Nat. Nanotechnol.* **2017**, *12* (3), 194–206.
- (2) Liu, J.; Bao, Z.; Cui, Y.; Dufek, E. J.; Goodenough, J. B.; Khalifah, P.; Li, Q.; Liaw, B. Y.; Liu, P.; Manthiram, A.; et al. Pathways for practical high-energy long-cycling lithium metal batteries. *Nature Energy* **2019**, *4* (3), 180–186.
- (3) Park, J. B.; Choi, C.; Yu, S.; Chung, K. Y.; Kim, D. W. Porous Lithiophilic Li–Si Alloy-Type Interfacial Framework via Self-Discharge Mechanism for Stable Lithium Metal Anode with Superior Rate. *Adv. Energy Mater.* **2021**, *11* (37), 2101544.
- (4) Sun, X.; Zhang, X.; Ma, Q.; Guan, X.; Wang, W.; Luo, J. Revisiting the Electroplating Process for Lithium-Metal Anodes for Lithium-Metal Batteries. *Angew. Chem., Int. Ed. Engl.* **2020**, *59* (17), 6665–6674.
- (5) Zhao, J.; Zhou, G.; Yan, K.; Xie, J.; Li, Y.; Liao, L.; Jin, Y.; Liu, K.; Hsu, P. C.; Wang, J.; et al. Air-stable and freestanding lithium alloy/graphene foil as an alternative to lithium metal anodes. *Nat. Nanotechnol.* **2017**, *12* (10), 993–999.
- (6) Li, X.; Lv, M.; Tian, Y.; Gao, L.; Liu, T.; Zhou, Q.; Xu, Y.; Shen, L.; Shi, W.; Li, X. Negatively charged polymeric interphase for regulated uniform lithium-ion transport in stable lithium metal batteries. *Nano Energy* **2021**, *87*, 106214.

- (7) Wang, H.; Liu, Y.; Li, Y.; Cui, Y. Lithium Metal Anode Materials Design: Interphase and Host. *Electrochem. Energy Rev.* **2019**, *2* (4), 509–517.
- (8) Chen, H.; Yang, Y.; Boyle, D. T.; Jeong, Y. K.; Xu, R.; de Vasconcelos, L. S.; Huang, Z.; Wang, H.; Wang, H.; Huang, W.; et al. Free-standing ultrathin lithium metal–graphene oxide host foils with controllable thickness for lithium batteries. *Nature Energy* **2021**, *6* (8), 790–798.
- (9) Liu, S.; Ji, X.; Yue, J.; Hou, S.; Wang, P.; Cui, C.; Chen, J.; Shao, B.; Li, J.; Han, F.; et al. High Interfacial-Energy Interphase Promoting Safe Lithium Metal Batteries. *J. Am. Chem. Soc.* **2020**, *142* (5), 2438–2447.
- (10) Kim, S.; Park, S. O.; Lee, M.-Y.; Lee, J.-A.; Kristanto, I.; Lee, T. K.; Hwang, D.; Kim, J.; Wi, T.-U.; Lee, H.-W.; et al. Stable electrode–electrolyte interfaces constructed by fluorine- and nitrogen-donating ionic additives for high-performance lithium metal batteries. *Energy Storage Mater.* **2022**, *45*, 1–13.
- (11) Piao, N.; Liu, S.; Zhang, B.; Ji, X.; Fan, X.; Wang, L.; Wang, P.-F.; Jin, T.; Liou, S.-C.; Yang, H.; et al. Lithium Metal Batteries Enabled by Synergetic Additives in Commercial Carbonate Electrolytes. *ACS Energy Lett.* **2021**, *6* (5), 1839–1848.
- (12) Zhao, Q.; Utomo, N. W.; Kocem, A. L.; Jin, S.; Deng, Y.; Zhu, V. X.; Moganty, S.; Coates, G. W.; Archer, L. A. Upgrading Carbonate Electrolytes for Ultra-stable Practical Lithium Metal Batteries. *Angew. Chem., Int. Ed. Engl.* **2022**, *61* (9), No. e202116214.
- (13) Wang, C.; Adair, K.; Sun, X. All-Solid-State Lithium Metal Batteries with Sulfide Electrolytes: Understanding Interfacial Ion and Electron Transport. *Acc. Mater. Res.* **2022**, *3* (1), 21–32.
- (14) Dong, L.; Zhong, S.; Yuan, B.; Ji, Y.; Liu, J.; Liu, Y.; Yang, C.; Han, J.; He, W. Electrolyte Engineering for High-Voltage Lithium Metal Batteries. *Research* **2022**, *2022*, 1–52.
- (15) Ugata, Y.; Shigenobu, K.; Tataru, R.; Ueno, K.; Watanabe, M.; Dokko, K. Solvate electrolytes for Li and Na batteries: structures, transport properties, and electrochemistry. *Phys. Chem. Chem. Phys.* **2021**, *23* (38), 21419–21436.
- (16) Zheng, J.; Lochala, J. A.; Kwok, A.; Deng, Z. D.; Xiao, J. Research Progress towards Understanding the Unique Interfaces between Concentrated Electrolytes and Electrodes for Energy Storage Applications. *Adv. Sci.* **2017**, *4* (8), 1700032.
- (17) Chen, J.; Fan, X.; Li, Q.; Yang, H.; Khoshi, M. R.; Xu, Y.; Hwang, S.; Chen, L.; Ji, X.; Yang, C.; et al. Electrolyte design for LiF-rich solid–electrolyte interfaces to enable high-performance micro-sized alloy anodes for batteries. *Nature Energy* **2020**, *5* (5), 386–397.
- (18) Li, T.; Zhang, X.-Q.; Shi, P.; Zhang, Q. Fluorinated Solid-Electrolyte Interphase in High-Voltage Lithium Metal Batteries. *Joule* **2019**, *3* (11), 2647–2661.
- (19) Qian, J.; Henderson, W. A.; Xu, W.; Bhattacharya, P.; Engelhard, M.; Borodin, O.; Zhang, J. G. High rate and stable cycling of lithium metal anode. *Nat. Commun.* **2015**, *6*, 6362.
- (20) Wang, J.; Yamada, Y.; Sodeyama, K.; Chiang, C. H.; Tateyama, Y.; Yamada, A. Superconcentrated electrolytes for a high-voltage lithium-ion battery. *Nat. Commun.* **2016**, *7*, 12032.
- (21) Li, T.; Li, Y.; Sun, Y.; Qian, Z.; Wang, R. New Insights on the Good Compatibility of Ether-Based Localized High-Concentration Electrolyte with Lithium Metal. *ACS Mater. Lett.* **2021**, *3* (6), 838–844.
- (22) Lin, S.; Hua, H.; Li, Z.; Zhao, J. Functional Localized High-Concentration Ether-Based Electrolyte for Stabilizing High-Voltage Lithium-Metal Battery. *ACS Appl. Mater. Interfaces* **2020**, *12* (30), 33710–33718.
- (23) Ren, X.; Zou, L.; Cao, X.; Engelhard, M. H.; Liu, W.; Burton, S. D.; Lee, H.; Niu, C.; Matthews, B. E.; Zhu, Z.; et al. Enabling High-Voltage Lithium-Metal Batteries under Practical Conditions. *Joule* **2019**, *3* (7), 1662–1676.
- (24) Xia, L.; Lee, S.; Jiang, Y.; Li, S.; Liu, Z.; Yu, L.; Hu, D.; Wang, S.; Liu, Y.; Chen, G. Z. Physicochemical and Electrochemical Properties of 1,1,2,2-Tetrafluoroethyl-2,2,3,3-Tetrafluoropropyl Ether as a Co-Solvent for High-Voltage Lithium-Ion Electrolytes. *ChemElectroChem.* **2019**, *6* (14), 3747–3755.
- (25) Chen, Y.; Yu, Z.; Rudnicki, P.; Gong, H.; Huang, Z.; Kim, S. C.; Lai, J. C.; Kong, X.; Qin, J.; Cui, Y.; et al. Steric Effect Tuned Ion Solvation Enabling Stable Cycling of High-Voltage Lithium Metal Battery. *J. Am. Chem. Soc.* **2021**, *143* (44), 18703–18713.
- (26) Pham, T. D.; Bin Faheem, A.; Kim, J.; Oh, H. M.; Lee, K. K. Practical High-Voltage Lithium Metal Batteries Enabled by Tuning the Solvation Structure in Weakly Solvating Electrolyte. *Small* **2022**, *18* (14), No. 2107492.
- (27) Wang, H.; Yu, Z.; Kong, X.; Huang, W.; Zhang, Z.; Mackanic, D. G.; Huang, X.; Qin, J.; Bao, Z.; Cui, Y. Dual-Solvent Li-Ion Solvation Enables High-Performance Li-Metal Batteries. *Adv. Mater.* **2021**, *33* (25), No. 2008619.
- (28) Wang, Z.; Wang, H.; Qi, S.; Wu, D.; Huang, J.; Li, X.; Wang, C.; Ma, J. Structural regulation chemistry of lithium ion solvation for lithium batteries. *EcoMat* **2022**, *4* (4), e12200 DOI: 10.1002/eom2.12200.
- (29) Chernyak, Y. Dielectric Constant, Dipole Moment, and Solubility Parameters of Some Cyclic Acid Esters. *J. Chem. Eng. Data* **2006**, *51* (2), 416–418.
- (30) Griffiths, T. R.; Pugh, D. C. Correlations among solvent polarity scales, dielectric constant and dipole moment, and a means to reliable predictions of polarity scale values from current data. *Coord. Chem. Rev.* **1979**, *29* (2–3), 129–211.
- (31) Pham, T. D.; Lee, K. K. Simultaneous Stabilization of the Solid/Cathode Electrolyte Interface in Lithium Metal Batteries by a New Weakly Solvating Electrolyte. *Small* **2021**, *17* (20), No. 2100133.
- (32) Yao, Y. X.; Chen, X.; Yan, C.; Zhang, X. Q.; Cai, W. L.; Huang, J. Q.; Zhang, Q. Regulating Interfacial Chemistry in Lithium-Ion Batteries by a Weakly Solvating Electrolyte. *Angew. Chem., Int. Ed. Engl.* **2021**, *60* (8), 4090–4097.
- (33) Cui, L.; Yang, G. P.; Wu, W. P.; Miao, H. H.; Shi, Q. Z.; Wang, Y. Y. Solvents and auxiliary ligands co-regulate three antiferromagnetic Co(II) MOFs based on a semi-rigid carboxylate ligand. *Dalton Trans* **2014**, *43* (15), 5823–5830.
- (34) Yu, Z.; Wang, H.; Kong, X.; Huang, W.; Tsao, Y.; Mackanic, D. G.; Wang, K.; Wang, X.; Huang, W.; Choudhury, S.; et al. Molecular design for electrolyte solvents enabling energy-dense and long-cycling lithium metal batteries. *Nature Energy* **2020**, *5* (7), 526–533.
- (35) Adams, B. D.; Zheng, J.; Ren, X.; Xu, W.; Zhang, J. G. Accurate Determination of Coulombic Efficiency for Lithium Metal Anodes and Lithium Metal Batteries. *Adv. Energy Mater.* **2017**, *8* (7), 1702097.
- (36) Chen, S.-P.; Lv, D.; Chen, J.; Zhang, Y.-H.; Shi, F.-N. Review on Defects and Modification Methods of LiFePO<sub>4</sub> Cathode Material for Lithium-Ion Batteries. *Energy Fuels* **2022**, *36* (3), 1232–1251.
- (37) Yuan, L.-X.; Wang, Z.-H.; Zhang, W.-X.; Hu, X.-L.; Chen, J.-T.; Huang, Y.-H.; Goodenough, J. B. Development and challenges of LiFePO<sub>4</sub> cathode material for lithium-ion batteries. *Energy Environ. Sci.* **2011**, *4* (2), 269–284.
- (38) Xia, C.; Kwok, C. Y.; Nazar, L. F. A high-energy-density lithium-oxygen battery based on a reversible four-electron conversion to lithium oxide. *Science* **2018**, *361* (6404), 777–781.
- (39) Zhou, M.-Y.; Ding, X.-Q.; Ding, J.-F.; Hou, L.-P.; Shi, P.; Xie, J.; Li, B.-Q.; Huang, J.-Q.; Zhang, X.-Q.; Zhang, Q. Quantifying the apparent electron transfer number of electrolyte decomposition reactions in anode-free batteries. *Joule* **2022**, *6*, 2122.
- (40) Barr, T. L.; Seal, S. Nature of the use of adventitious carbon as a binding energy standard. *J. Vac. Sci. Technol. A* **1995**, *13* (3), 1239–1246.
- (41) Miller, D. J.; Biesinger, M. C.; McIntyre, N. S. Interactions of CO<sub>2</sub> and CO at fractional atmosphere pressures with iron and iron oxide surfaces: one possible mechanism for surface contamination? *Surf. Interface Anal.* **2002**, *33* (4), 299–305.
- (42) Swift, P. Adventitious carbon—the panacea for energy referencing? *Surf. Interface Anal.* **1982**, *4* (2), 47–51.
- (43) Jiang, M.; Danilov, D. L.; Eichel, R. A.; Notten, P. H. L. A Review of Degradation Mechanisms and Recent Achievements for Ni-

Rich Cathode-Based Li-Ion Batteries. *Adv. Energy Mater.* **2021**, No. 48, 2103005.

(44) Li, T.; Yuan, X.-Z.; Zhang, L.; Song, D.; Shi, K.; Bock, C. Degradation Mechanisms and Mitigation Strategies of Nickel-Rich NMC-Based Lithium-Ion Batteries. *Electrochem. Energy Rev.* **2020**, *3* (1), 43–80.

(45) Chen, J.; Yang, H.; Li, T.; Liu, C.; Tong, H.; Chen, J.; Liu, Z.; Xia, L.; Chen, Z.; Duan, J.; et al. The Effects of Reversibility of H2-H3 Phase Transition on Ni-Rich Layered Oxide Cathode for High-Energy Lithium-Ion Batteries. *Front Chem.* **2019**, *7*, 500.

(46) Ryu, H.-H.; Park, K.-J.; Yoon, C. S.; Sun, Y.-K. Capacity Fading of Ni-Rich Li[Ni<sub>x</sub>Co<sub>y</sub>Mn<sub>1-x-y</sub>]O<sub>2</sub> (0.6 ≤ x ≤ 0.95) Cathodes for High-Energy-Density Lithium-Ion Batteries: Bulk or Surface Degradation? *Chem. Mater.* **2018**, *30* (3), 1155–1163.

(47) Zhang, S. S. Problems and their origins of Ni-rich layered oxide cathode materials. *Energy Storage Mater.* **2020**, *24*, 247–254.

(48) Gerold, E.; Schinnerl, C.; Antrekowitsch, H. Critical Evaluation of the Potential of Organic Acids for the Environmentally Friendly Recycling of Spent Lithium-Ion Batteries. *Recycling* **2022**, *7* (1), 4.

(49) Meshram, P.; Pandey, B. D.; Mankhand, T. R. Extraction of lithium from primary and secondary sources by pre-treatment, leaching and separation: A comprehensive review. *Hydrometallurgy* **2014**, *150*, 192–208.

(50) Wachs, S. J.; Behling, C.; Ranninger, J.; Müller, J.; Mayrhofer, K. J. J.; Berkes, B. B. Online Monitoring of Transition-Metal Dissolution from a High-Ni-Content Cathode Material. *ACS Appl. Mater. Interfaces* **2021**, *13* (28), 33075–33082.

(51) Hirata, K.; Kawase, T.; Sumida, Y. Passivation Behavior of Aluminum in a Carbonate-Free Electrolyte Based on Lithium Bis(fluorosulfonyl)imide and Sulfolane. *J. Electrochem. Soc.* **2020**, *167* (14), 140534.

(52) Li, C.-I.; Zeng, S.-w.; Wang, P.; Li, Z.-j.; Yang, L.; Zhao, D.-n.; Wang, J.; Liu, H.-n.; Li, S.-y. Mechanism of aluminum corrosion in LiFSI-based electrolyte at elevated temperatures. *Transactions of Nonferrous Metals Society of China* **2021**, *31* (5), 1439–1451.

(53) Ma, T.; Xu, G. L.; Li, Y.; Wang, L.; He, X.; Zheng, J.; Liu, J.; Engelhard, M. H.; Zapol, P.; Curtiss, L. A.; et al. Revisiting the Corrosion of the Aluminum Current Collector in Lithium-Ion Batteries. *J. Phys. Chem. Lett.* **2017**, *8* (5), 1072–1077.

(54) Meister, P.; Qi, X.; Kloepsch, R.; Kramer, E.; Streipert, B.; Winter, M.; Placke, T. Anodic Behavior of the Aluminum Current Collector in Imide-Based Electrolytes: Influence of Solvent, Operating Temperature, and Native Oxide-Layer Thickness. *ChemSusChem* **2017**, *10* (4), 804–814.

(55) Wang, X.; Yasukawa, E.; Mori, S. Inhibition of anodic corrosion of aluminum cathode current collector on recharging in lithium imide electrolytes. *Electrochim. Acta* **2000**, *45* (17), 2677–2684.

(56) Nan, B.; Chen, L.; Rodrigo, N. D.; Borodin, O.; Piao, N.; Xia, J.; Pollard, T.; Hou, S.; Zhang, J.; Ji, X.; et al. Enhancing Li<sup>+</sup> Transport in NMC811||Graphite Lithium-Ion Batteries at Low Temperatures by Using Low-Polarity-Solvent Electrolytes. *Angew. Chem., Int. Ed. Engl.* **2022**, *61* (35), No. e202205967.

(57) Liu, J.; Yuan, B.; Dong, L.; Zhong, S.; Ji, Y.; Liu, Y.; Han, J.; Yang, C.; He, W. Constructing Low-Solvation Electrolytes for Next-Generation Lithium-Ion Batteries. *Batteries & Supercaps* **2022**, *5* (10), e202200256 DOI: 10.1002/batt.202200256.

(58) Yan, C.; Jiang, L. L.; Yao, Y. X.; Lu, Y.; Huang, J. Q.; Zhang, Q. Nucleation and Growth Mechanism of Anion-Derived Solid Electrolyte Interphase in Rechargeable Batteries. *Angew. Chem., Int. Ed. Engl.* **2021**, *60* (15), 8521–8525.

(59) Yang, Y.; Fang, Z.; Yin, Y.; Cao, Y.; Wang, Y.; Dong, X.; Xia, Y. Synergy of Weakly-Solvated Electrolyte and Optimized Interphase Enables Graphite Anode Charge at Low Temperature. *Angew. Chem., Int. Ed. Engl.* **2022**, *61* (36), No. e202208345.

## Recommended by ACS

### Weakly Solvating Cyclic Ether Electrolyte for High-Voltage Lithium Metal Batteries

Jiaming Zhang, Haiyan Wang, et al.

MARCH 13, 2023  
ACS ENERGY LETTERS

READ 

### Cage Dynamics-Mediated High Ionic Transport in Li-O<sub>2</sub> Batteries with a Hybrid Aprotic Electrolyte: LiTFSI, Sulfolane, and N,N-Dimethylacetamide

and Bhabani S. Mallik

MARCH 24, 2023  
THE JOURNAL OF PHYSICAL CHEMISTRY B

READ 

### Nonflammable Fluorinated Ester-Based Electrolytes for Safe and High-Energy Batteries with LiCoO<sub>2</sub>

Yosuke Ugata, Naoaki Yabuuchi, et al.

APRIL 25, 2023  
CHEMISTRY OF MATERIALS

READ 

### High-Voltage-Compatible Dual-Ether Electrolyte for Lithium Metal Batteries

Jihyun Jang, Junyoung Mun, et al.

SEPTEMBER 14, 2021  
ACS APPLIED ENERGY MATERIALS

READ 

Get More Suggestions >